

SOLAR CELLS

Reconfiguring the band-edge states of photovoltaic perovskites by conjugated organic cations

Jingjing Xue^{1*}, Rui Wang^{1*}, Xihan Chen^{2*}, Cangliang Yao³, Xiaoyun Jin⁴, Kai-Li Wang⁵, Wenchao Huang⁶, Tianyi Huang¹, Yepin Zhao¹, Yaxin Zhai², Dong Meng¹, Shaun Tan¹, Ruzhang Liu⁴, Zhao-Kui Wang⁵, Chenhui Zhu⁷, Kai Zhu², Matthew C. Beard^{2†}, Yanfa Yan^{3†}, Yang Yang^{1†}

The band edges of metal-halide perovskites with a general chemical structure of ABX_3 (A, usually a monovalent organic cation; B, a divalent cation; and X, a halide anion) are constructed mainly of the orbitals from B and X sites. Hence, the structural and compositional varieties of the inorganic B–X framework are primarily responsible for regulating their electronic properties, whereas A-site cations are thought to only help stabilize the lattice and not to directly contribute to near-edge states. We report a π -conjugation-induced extension of electronic states of A-site cations that affects perovskite frontier orbitals. The π -conjugated pyrene-containing A-site cations electronically contribute to the surface band edges and influence the carrier dynamics, with a properly tailored intercalation distance between layers of the inorganic framework. The ethylammonium pyrene increased hole mobilities, improved power conversion efficiencies relative to that of a reference perovskite, and enhanced device stability.

The band-edge electronic structure of hybrid metal-halide perovskites (ABX_3 , where A is usually a monovalent organic cation, B is a divalent cation, and X is a halide anion) develops from the orbitals of B and X sites (1) and can be tuned through the compositional and structural flexibility of the B–X framework (2–12). By contrast, the A-site cations are generally not thought to directly affect electronic structure near the band edges because their electronic states lie far from the inorganic band edges (13). Instead, different A-site cation sizes can induce indirect effects by causing structural deformation of the inorganic B–X framework, such as unit volume variation, octahedral distortion, and dimensional reduction (14–17). We now show that the electronic states of the A-site cations can be extended and directly contribute to the frontier orbitals of the hybrid perovskite through a combination of a large π -conjugated structure and a tailored intercalation distance between layers of the inorganic framework, which provides additional degrees of electronic tunability to near-edge electronic configuration. The carrier dynamics could be rationally

tuned in accordance with the device architecture by modifying the A-site organic structure.

We designed a polycyclic aromatic tail with large π -conjugation that was attached to an ammonium A-site cation. The chemical structures of the as-synthesized organic cations featured different lengths of the tethering alkylammonium group—namely PRA, PRMA, and PREA for pyrene-based ammonium, methylammonium, and ethylammonium, respectively (Fig. 1A; see synthesis details in supplementary text S1). When these organic cations were assembled with the inorganic framework, the extent to which the positively charged ammonium head group intercalated into the octahedral cavity depended on the length of the bridging alkyl chain. Electron delocalization in the large conjugated pyrene structure lowered the frontier orbital separation of the organic molecule and enabled orbital overlap with the inorganic moiety (18).

The alkyl chain length affected the electronic interaction between the two moieties. Ultraviolet photoemission spectroscopy of PRMA and PREA cations assembled onto the surface of the Pb–I framework of a formamidinium-based perovskite thin film (Fig. 1B) revealed additional electronic states near the tail of the valence band (the Fermi energy has been aligned for better comparison). However, a perovskite thin film with the PRA moieties attached exhibited similar band-tail characteristics to that of the reference, indicating a lack of electronic contribution from PRA to the surface band edges.

First-principles calculations of the partial density of states revealed electronic states near the surface band edges (Fig. 1C). As the alkyl chain of the ammonium group became longer, the electronic states from the organic components at the valence band were pushed to a higher energy level. The electronic states from PRA were as much as 0.34 eV below the valence

band maximum (VBM), but PRMA and PREA had electronic states near the VBM. The distribution of the electronic states of the organic ammonium cations with respect to the inorganic band structure (Fig. 1D) showed that the orbitals of PRMA and PREA greatly overlapped with the inorganic VBM, with the highest unoccupied orbitals only 0.02 eV below and 0.01 eV above the VBM, respectively. Thus, the band structure of PRA resembled that of the reference film, with the VBM consisting of I 5p and Pb 6s orbitals. However, for PRMA and PREA, the VBM had contributions from the orbitals of both inorganic and organic components. The participation of PRMA and PREA in the surface band-edge construction was also observed in all-inorganic $CsPbI_2Br$ perovskite (supplementary text S2), indicating the generality of this concept.

The discrepancy in the surface band-edge configuration originated from different chemical interaction modes between the inorganic framework and the ammonium cations with different alkyl chain lengths; theoretical modeling of the assembly of these organic ammoniums on the surface of the Pb–I framework is shown in Fig. 2A. We used time-of-flight secondary-ion mass spectrometry and grazing-angle polarization-dependent infrared reflection-absorption spectroscopy to verify the vertical assembly of the ammonium cations on the surface (supplementary text S2 and S3). Both PRMA and PREA could anchor into the octahedral cavity through electrostatic interactions between the ammonium cations and the PbI_6^{2-} octahedra. However, PRMA, which has a shorter alkyl chain length between the ammonium head and the pyrene tail, exhibited a distorted intercalation configuration because of the structural rigidity and pronounced steric hindrance induced by the pyrene ring.

The elongated alkyl chain in PREA enabled more flexibility with less steric hindrance and displayed almost vertical intercalation of PREA into the inorganic layers. The conjugated tails of PREA were stacked nearly perpendicular to the plane of the inorganic layer. With a reduction in the length of the tethering alkylammonium group, the orientation of PRMA tilted away from the vertical direction by $\sim 30^\circ$, which disrupted the π - π stacking and reduced the electronic delocalization. By contrast, PRA, which lacked a flexible alkyl chain, failed to relieve the steric hindrance of the pyrene group when anchoring into the Pb–I framework. Its binding mode to the inorganic surface would be more accurately described as adsorption rather than anchoring, as also evidenced by the vertically oriented pyrene tail in PRA stacking. With a shallow interaction depth, the steric hindrance from the large pyrene tail no longer affects the intercalation configuration, enabling a molecular orientation driven by the surface energy and π - π stacking.

¹Department of Materials Science and Engineering and California NanoSystems Institute, University of California, Los Angeles, CA 90095, USA. ²National Renewable Energy Laboratory, Golden, CO 80401, USA. ³Department of Physics and Astronomy and Center for Photovoltaics Innovation and Commercialization, The University of Toledo, Toledo, OH 43606, USA. ⁴School of Chemistry and Chemical Engineering, Yangzhou University, Yangzhou 225002, China. ⁵Institute of Functional Nano & Soft Materials (FUNSOM), Jiangsu Key Laboratory for Carbon-Based Functional Materials & Devices, Soochow University, Suzhou 215123, China. ⁶Department of Materials Science and Engineering, Monash University, Clayton, VIC, 3800, Australia. ⁷Advanced Light Source, Lawrence Berkeley National Laboratory, Berkeley, CA 94720, USA.

*These authors contributed equally to this work.

†Corresponding author. Email: matt.beard@nrel.gov (M.C.B.); yanfa.yan@utoledo.edu (Y.Yan); yangy@ucla.edu (Y.Yang)

We used attenuated total reflection–Fourier transform infrared (ATR-FTIR) spectroscopy to investigate the chemical binding between the organic cations and the Pb-I framework. Difference ATR-FTIR spectra of perovskite

films with PRA, PRMA, and PREA with respect to the reference film are shown in Fig. 2B. Distinctive vibration features from the reference and PRA samples were observed in PRMA and PREA samples between 900 to

1100 cm^{-1} . Both PRMA and PREA showed substantially reduced absorption near 930 cm^{-1} and increased absorption near 1060 cm^{-1} , which we attributed to the change of the out-of-plane N-H wagging and C-N stretching

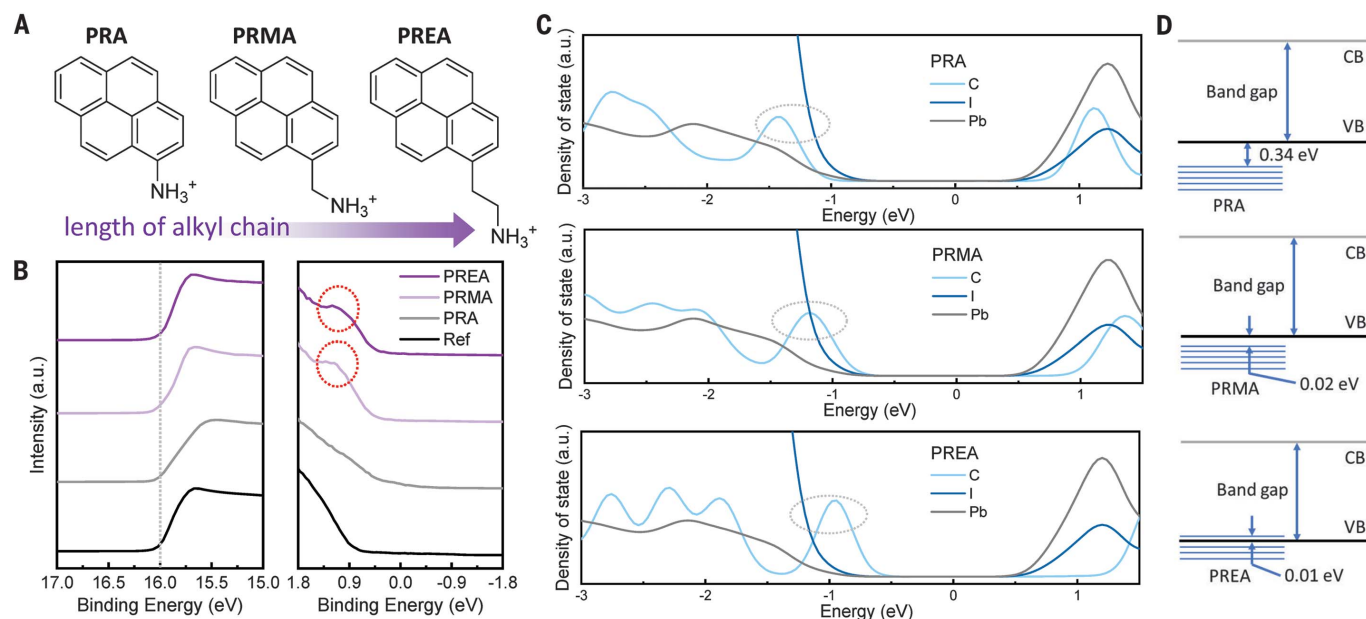


Fig. 1. Surface band-edge structures with the electronic contribution from conjugated A-site cations. (A) Chemical structures of three different organic ammoniums featuring different lengths of tethering alkylammonium. (B) Ultraviolet photoemission spectroscopy results. The vertical dashed line indicates the aligned

Fermi energy; dashed circles indicate the additional electronic states. a.u., arbitrary units. (C and D) Calculated partial density of states (C) and band diagrams (D) of perovskites with PRA, PRMA, and PREA. Dashed ovals indicate the electronic states near the surface band edges. CB, conduction band; VB, valence band.

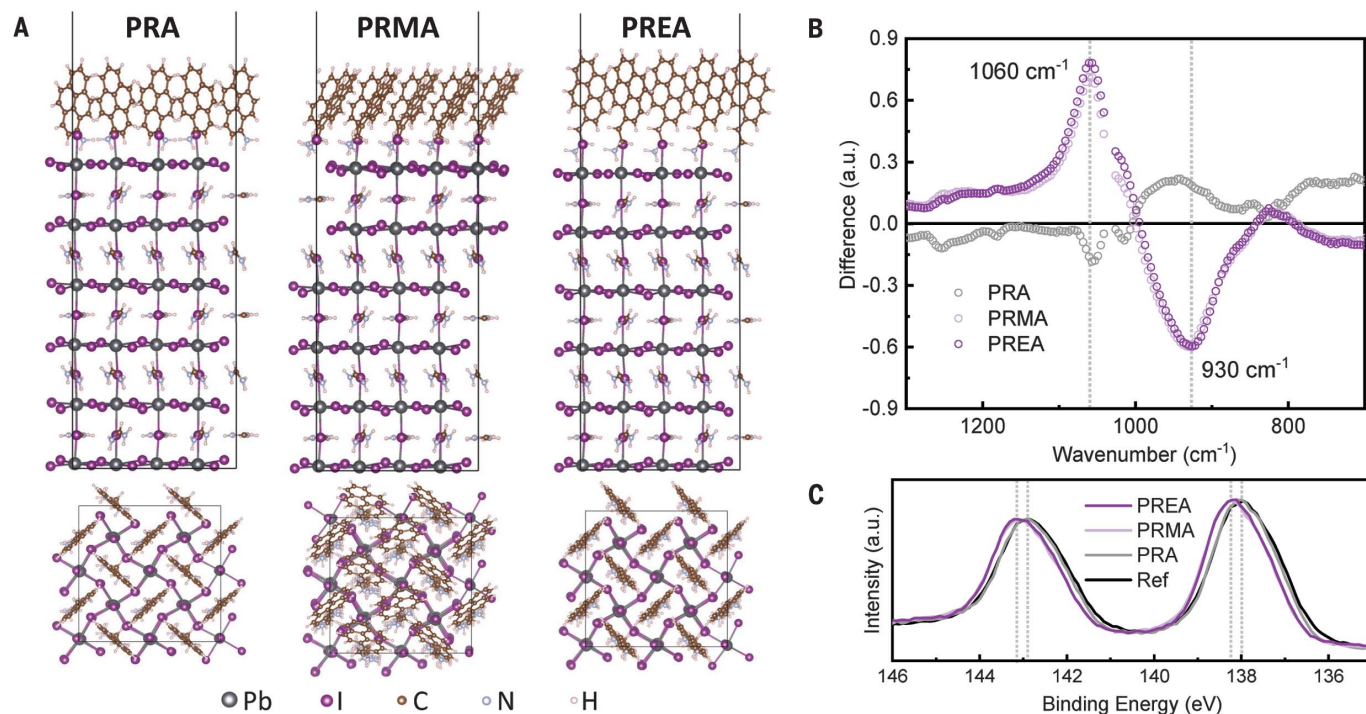


Fig. 2. Interaction modes between the conjugated ammoniums and the perovskite framework. (A) Side view (top) and top view (bottom) of intercalation configuration modeled by density functional theory (DFT) for PRA, PRMA, and

PREA. (B) Difference ATR spectra of perovskite with PRA, PRMA, and PREA with respect to the reference sample. (C) XPS data for Pb 4f 7/2 and Pb 4f 5/2 core-level spectra for perovskite with PRA, PRMA, and PREA.

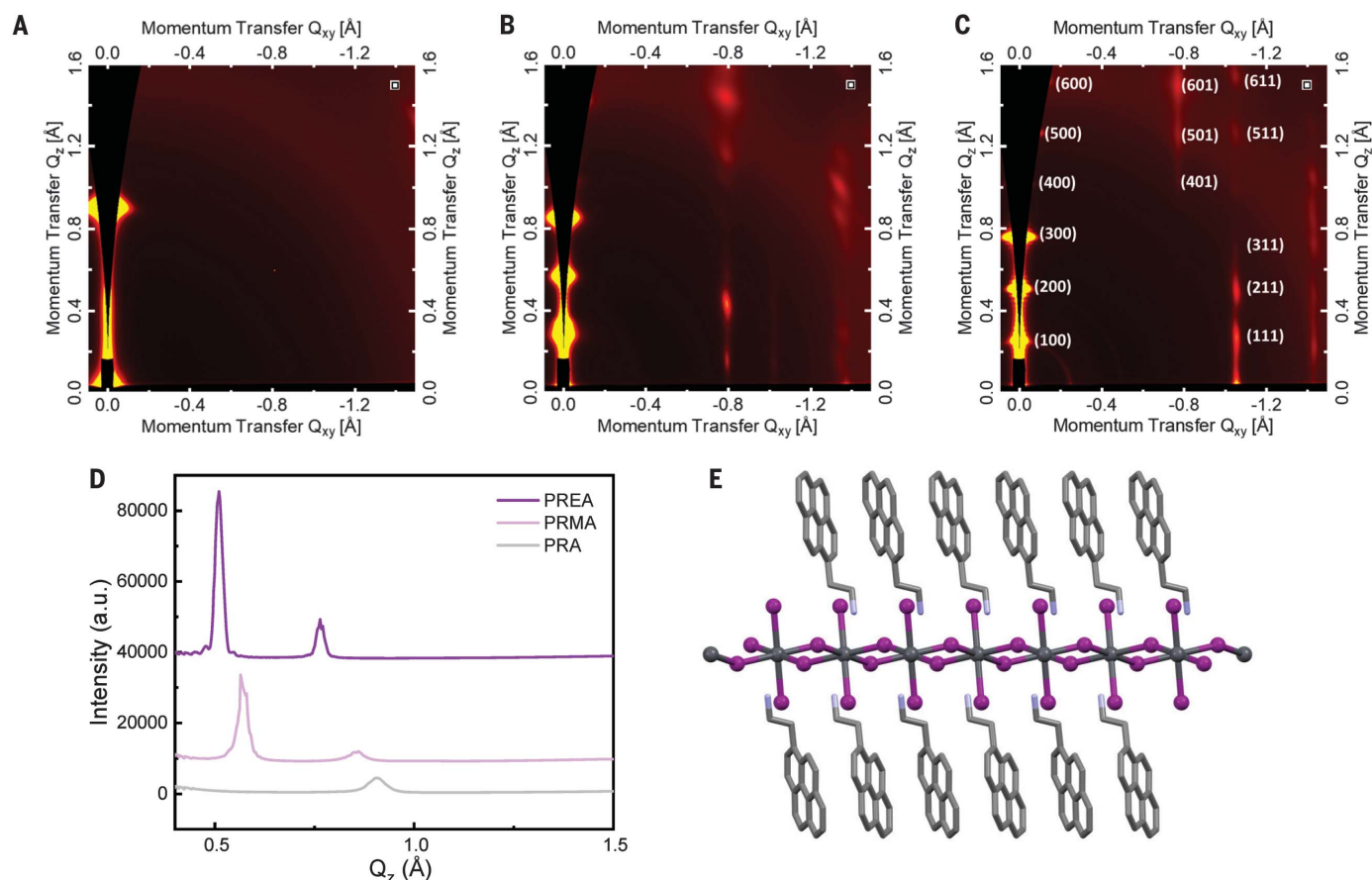


Fig. 3. Intercalation configuration of the conjugated ammoniums. (A to C) GIWAXS patterns of perovskite thin films when PbI_2 is stoichiometrically mixed with (A) PRA, (B) PRMA, and (C) PREA salt, respectively, to form a 2D perovskite phase. (D) Out-of-plane GIWAXS profiles for PRA-, PRMA-, and PREA-based samples. (E) Crystal structure of a 2D $\text{PREA}_2\text{PbI}_4$ perovskite single crystal.

modes, respectively. The absence of distinctive vibration features in PRA samples indicated a different binding mode with a weak interaction. High-resolution x-ray photoemission spectroscopy (XPS) of the Pb 4f orbital for the perovskite film with different ammonium cations (Fig. 2C) showed two main peaks at ~ 138 and ~ 143 eV, corresponding to the Pb 4f $7/2$ and Pb 4f $5/2$ orbitals, respectively (19). The peaks from Pb 4f shifted to higher binding energies in the film with PRMA and PREA, whereas the spectra of PRA samples remained almost identical to that of the reference sample. This difference suggested a stronger interaction between PRMA or PREA and Pb, as well as a more profound influence on the bonding character of Pb in the inorganic framework, compared with that in the case of PRA.

The dense and periodic insertion of the pyrene-based ammoniums into the Pb-I framework was further evaluated by grazing-incident wide-angle x-ray scattering (GIWAXS) and the growth of two-dimensional (2D) perovskite single crystals. The GIWAXS patterns of perovskite thin films generated by stoichiometrically mixing PbI_2 and PRA, PRMA, or PREA salt to form a 2D perovskite phase are shown in

Fig. 3, A to C, respectively. Both PRMA- and PREA-based perovskite samples exhibited out-of-plane diffraction patterns of $\{100\}$ planes, indicating the formation of 2D perovskite phases, but this diffraction feature was absent for PRA, confirming that it failed to anchor into the Pb-I framework. The PREA-based 2D perovskite showed much higher crystallinity and preferred out-of-plane crystallographic orientation than PRMA perovskites (Fig. 3D), further verifying the distorted intercalation configuration of PRMA. Single crystals of PREA-based 2D perovskite showed the periodic stacking mode of the pyrene-based ammonium cations, and the pyrene rings had an edge-on packing with the Pb-I framework (Fig. 3E; see details of the crystal structures and the growth of single crystals in supplementary text S4).

The reconfiguration of the surface band-edge electronic structures involving A-site organic cations and the alkylammonium-controlled intercalation distance were also reflected in the change of surface carrier dynamics, which were probed by transient reflection spectroscopy (TRS) and time-resolved terahertz spectroscopy (TRTS) (20, 21). By modeling the measured surface carrier kinetics with a de-

finer surface interaction distance (see the modeling details in supplementary text S5), we could determine the binding configuration because the electronic interaction distance was related to the binding character between the organic ammonium cations and the inorganic moieties (Fig. 4A). The surface carrier kinetics probed by transient optical reflection for the cases of reference, PRA, PRMA, and PREA (Fig. 4B) revealed a $\sim 33\%$ increase in the interaction distance for PRMA or PREA relative to that for PRA (the absolute values may be longer than expected in the model, owing to the effects of film roughness). This increase in the interaction distance was consistent with the interaction mode between the organic ammonium cations and the perovskite lattice, where PRMA and PREA inserted into the lattice, unlike PRA.

The photoinduced electron and hole carrier mobilities are extracted by combining TRS and TRTS results. The surface photogenerated carrier transport was measured with the reflected optical probe (22) and provided information on the ambipolar diffusion coefficient (D_{ab}) (23, 24), whereas the terahertz probe pulse was sensitive to the sum of the

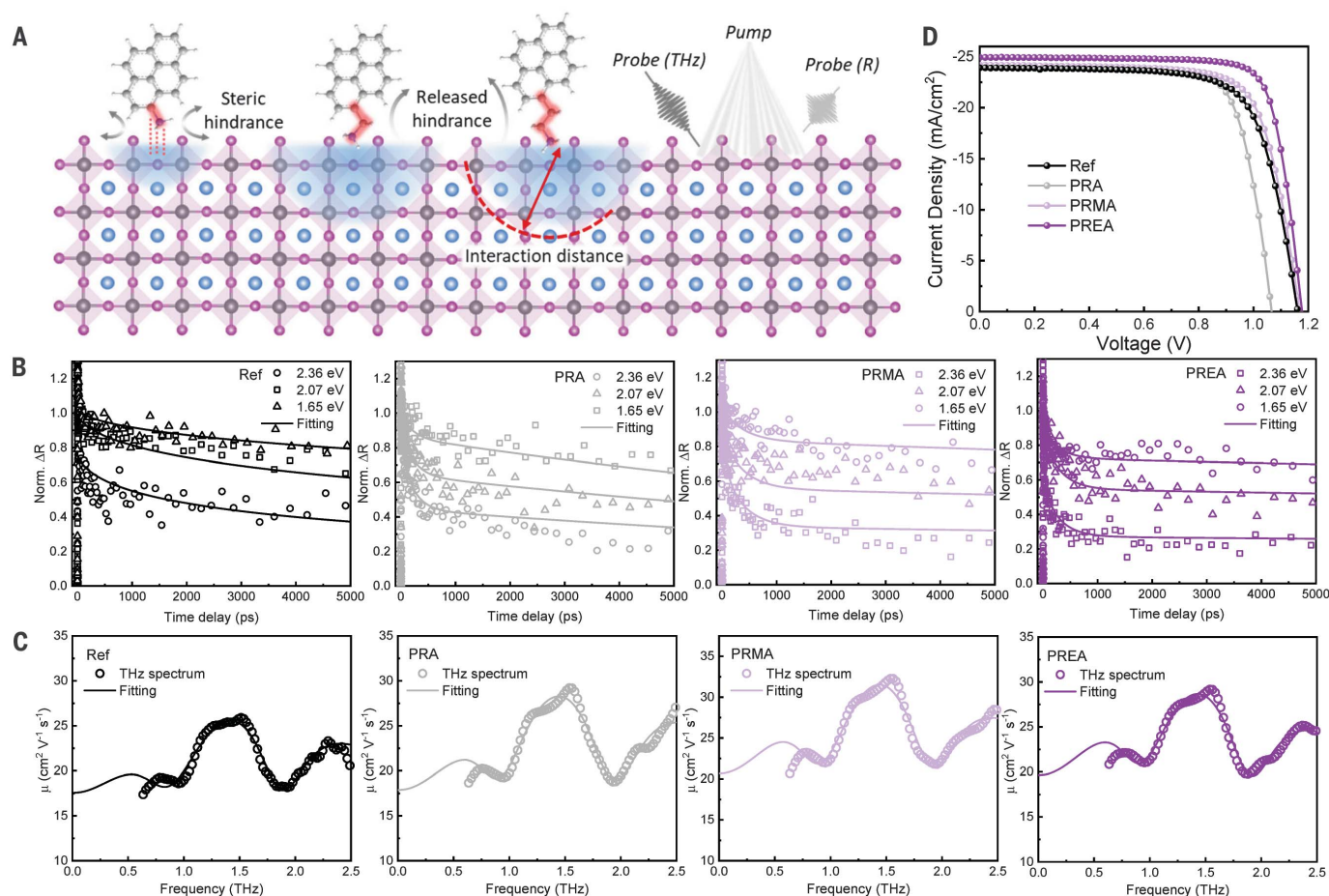


Fig. 4. Investigations on the change of carrier dynamics and photovoltaic response. (A) Schematic illustration of the influence of intercalation configuration and the interaction distance revealed by the combination of TRS and TRTS. R, reflection; THz, terahertz. (B) Surface-carrier kinetics pumped at 2.36, 2.07, and 1.65 eV probed by TRS and fitted with a diffusion model and

(C) TRTS spectra at 5-ps time delay and fitted with a Drude-Smith model for the reference sample and perovskite with PRA, PRMA, and PREA. (D) Current density–voltage curves of the as-fabricated perovskite solar cells, showing the influence of the changed band-edge configurations, and thus the carrier dynamics, on photovoltaic performance.

electron and hole mobilities $\sum \mu = \mu_e + \mu_h$ (20). By using the Einstein relation to determine the ambipolar mobility (μ_{ab}) from D_{ab} and combining it with $\sum \mu$, the individual mobilities of electrons μ_e and holes μ_h can be derived because $1/\mu_{ab} = (1/\mu_e) + (1/\mu_h)$. The sum of the dc mobility (μ_{dc}) was extracted by using a Drude-Smith model from transient terahertz spectra at 5-ps delay for reference, PRA, PRMA, and PREA (Fig. 4C; see modeling details in supplementary text S5). The best-fit parameters and the calculated carrier mobilities are summarized in table S1. Because the orbitals of the organic ammonium cations mainly interacted with the valence band of the inorganic lattice, the hole mobility was most substantially affected. The largest increase in hole mobility was observed for PREA; electron mobilities remained almost invariant across all samples.

The enhancement in hole mobility benefited the carrier collection in perovskite photovoltaic devices, as reflected by an increase in the short-circuit current (J_{sc}) and fill factor (FF). The

power conversion efficiency (PCE) of the as-fabricated perovskite solar cells with PREA exhibits the largest enhancement, from 20.1 to 23.0% (Fig. 4D). A smaller enhancement of hole mobility, and thus J_{sc} and FF, was observed for PRMA, which we attributed to the distorted intercalation of the ammonium cations generating energy disorder in the lattice. However, PRA actually led to a decrease in PCE because of a reduced open-circuit voltage that resulted from an unmatched energy level with the hole-transporting layer (supplementary text S3). Thus, rational control of the intercalation distance regulated by the tethering alkyl ammonium enabled electronic contribution of A-site cations to the near-edge band structure and, in turn, modified the carrier kinetics within devices. The insertion of the ammonium head into the framework, and thus the exposure of the hydrophobic polycyclic aromatic tail, further increased the stability of the devices. After 2000 hours of exposure to continuous light under open-circuit

conditions, the device with PREA maintained more than 85% of its original PCE, whereas the reference device degraded to only 60% of its initial PCE (supplementary text S6).

REFERENCES AND NOTES

- W. J. Yin, T. Shi, Y. Yan, *Appl. Phys. Lett.* **104**, 063903 (2014).
- J. S. Manser, J. A. Christians, P. V. Kamat, *Chem. Rev.* **116**, 12956–13008 (2016).
- W. Nie et al., *Science* **347**, 522–525 (2015).
- B. Saparov, D. B. Mitzi, *Chem. Rev.* **116**, 4558–4596 (2016).
- J. W. Lee, H. S. Kim, N. G. Park, *Acc. Chem. Res.* **49**, 311–319 (2016).
- B. Chen, P. N. Rudd, S. Yang, Y. Yuan, J. Huang, *Chem. Soc. Rev.* **48**, 3842–3867 (2019).
- D. Bi et al., *Nat. Energy* **1**, 16142 (2016).
- H. Zhang, M. K. Nazeeruddin, W. C. H. Choy, *Adv. Mater.* **31**, e1805702 (2019).
- R. Wang et al., *Adv. Funct. Mater.* **29**, 1808843 (2019).
- Y. Gao et al., *Nat. Chem.* **11**, 1151–1157 (2019).
- H. Min et al., *Science* **366**, 749–753 (2019).
- R. Wang et al., *Science* **366**, 1509–1513 (2019).
- W. J. Yin, J. H. Yang, J. Kang, Y. Yan, S. H. Wei, *J. Mater. Chem. A* **3**, 8926–8942 (2015).
- J.-W. Lee et al., *Nat. Commun.* **9**, 3021 (2018).
- H. Tsai et al., *Nature* **536**, 312–316 (2016).
- G. Grancini et al., *Nat. Commun.* **8**, 15684 (2017).

17. G. Grancini, M. K. Nazeeruddin, *Nat. Rev. Mater.* **4**, 4–22 (2019).
18. P. A. J. de Paula, *Physical Chemistry for the Life Sciences* (Oxford Univ. Press, 2006).
19. L. Wang *et al.*, *Science* **363**, 265–270 (2019).
20. Y. Zhai *et al.*, *ACS Energy Lett.* **5**, 47–55 (2020).
21. J. Tong *et al.*, *Science* **364**, 475–479 (2019).
22. W. Chu, Q. Zheng, O. V. Prezhdo, J. Zhao, W. A. Saidi, *Sci. Adv.* **6**, eaaw7453 (2020).
23. Y. Yang *et al.*, *Nat. Energy* **2**, 16207 (2017).
24. X. Chen, K. Wang, M. C. Beard, *Phys. Chem. Chem. Phys.* **21**, 16399–16407 (2019).

ACKNOWLEDGMENTS

Funding: This material is based on work supported by the U.S. Department of Energy's (DOE) Office of Energy Efficiency and Renewable Energy (EERE) under Solar Energy Technologies Office award DE-EE0008751. Work performed at the National Renewable Energy Laboratory and University of Toledo was supported as part of the Center for Hybrid Organic Inorganic Semiconductors for Energy (CHOISE), an Energy Frontier Research Center funded by the DOE Office of Basic Energy Sciences, under contract DE-AC36-08G028308, with Alliance for Sustainable Energy, LLC, the Manager and Operator of the National Renewable Energy

Laboratory. The views expressed in the article do not necessarily represent the views of the DOE or the U.S. government. All theoretical works were performed on National Renewable Energy Laboratory's Eagle Computing System and National Energy Research Scientific Computing Center. The work at the Yangzhou University was financially supported by the Priority Academic Program Development of Jiangsu Higher Education Institutions. Z.-K.W. acknowledges the Natural Science Foundation of China (91733301). This project was also supported by the Collaborative Innovation Center of Suzhou Nano Science and Technology. Part of the GIWAXS measurement was performed in beamline 7.3.3 at the Advanced Light Source, Lawrence Berkeley National Laboratory. The Australian Synchrotron, part of ANSTO, is also acknowledged for the GIWAXS characterizations. **Author contributions:** J.X. and R.W. conceived the idea, designed and conducted the experiments, and prepared the manuscript under the supervision of Y. Yang. X.C. designed and carried out the spectroscopy investigations and assisted with manuscript preparation under the supervision of M.C.B. Y. Zhai assisted with the spectroscopy measurement. C.Y. performed the DFT calculations under the supervision of Y. Yan. X.J., R.L., and J.X. designed and synthesized the materials. J.X., R.W., and D.M. synthesized and analyzed the single crystals. K.-L.W. assisted with the characterization of single crystals under the supervision of

Z.-K.W. T.H., S.T., and Y. Zhao assisted with the thin-film characterizations. C.Z., W.H., and R.W. performed the GIWAXS measurement. K.Z. contributed helpful discussion during the project. All authors discussed the results and commented on the manuscript.

Competing interests: The authors declare no competing interests.

Data and materials availability: All data are available in the main text or the supplementary materials. Crystallographic parameters for the structure of $\text{PREA}_2\text{PbI}_4$ are archived at the Cambridge Crystallographic Data Centre (www.ccdc.cam.ac.uk/) under reference number CCDC 2045757.

SUPPLEMENTARY MATERIALS

science.sciencemag.org/content/371/6529/636/suppl/DC1

Materials and Methods

Supplementary Text S1 to S6

Figs. S1 to S22

Tables S1 to S3

References (25–32)

[View/request a protocol for this paper from Bio-protocol.](#)

23 June 2020; resubmitted 4 December 2020

Accepted 5 January 2021

10.1126/science.abd4860

Reconfiguring the band-edge states of photovoltaic perovskites by conjugated organic cations

Jingjing XueRui WangXihan ChenCanglang YaoXiaoyun JinKai-Li WangWenchao HuangTianyi HuangYepin ZhaoYaxin ZhaiDong MengShaun TanRuzhang LiuZhao-Kui WangChenhui ZhuKai ZhuMatthew C. BeardYanfa YanYang Yang

Science, 371 (6529), • DOI: 10.1126/science.abd4860

A-sites join the band edge

The band edge of hybrid organic-inorganic perovskites, which have the general formula ABX₃, is mainly controlled by the inorganic X anions (such as chloride) and the B cation (such as lead). Organic A-site cations usually only exert indirect structural effects because their electronic levels lie far from the band edge. Xue *et al.* show that cations with large π -conjugated structures can interact with inorganic frontier molecular orbitals. A surface layer of ethylammonium pyrene, which had an optimal intercalation distance, increased hole mobilities and power conversion efficiencies relative to a reference inorganic perovskite and also improved device stability.

Science, this issue p. 636

View the article online

<https://www.science.org/doi/10.1126/science.abd4860>

Permissions

<https://www.science.org/help/reprints-and-permissions>

Use of this article is subject to the [Terms of service](#)